High-quality MOVPE butt-joint integration of InP/AlGaInAs/InGaAsP-based all-active optical components

Kulkova, Irina; Kadkhodazadeh, Shima; Kuznetsova, Nadezda; Huck, Alexander; Semenova, Elizaveta; Yvind, Kresten

Published in:
Journal of Crystal Growth

Link to article, DOI:
10.1016/j.jcrysgro.2014.06.026

Publication date:
2014

Document Version
Early version, also known as pre-print

www.elsevier.com/locate/jcrysgro

High-quality MOVPE butt-joint integration of InP/AlGaInAs/InGaAsP-based all-active optical components

I.V. Kulkova, S. Kadkhodazadeh, N. Kuznetsova, A. Huck, E.S. Semenova, K. Yvind

PII: S0022-0248(14)00410-2
DOI: http://dx.doi.org/10.1016/j.jcrysgro.2014.06.026
Reference: CRYS22297

To appear in: *Journal of Crystal Growth*

Received date: 10 April 2014
Revised date: 3 June 2014
Accepted date: 4 June 2014

Cite this article as: I.V. Kulkova, S. Kadkhodazadeh, N. Kuznetsova, A. Huck, E.S. Semenova, K. Yvind, High-quality MOVPE butt-joint integration of InP/AlGaInAs/InGaAsP-based all-active optical components, *Journal of Crystal Growth,* http://dx.doi.org/10.1016/j.jcrysgro.2014.06.026

High-quality MOVPE butt-joint integration of InP/AlGaInAs/InGaAsP-based all-active optical components

I. V. Kulkova[1,*], S. Kadkhodazadeh[2], N. Kuznetsova[1], A. Huck[3], E. S. Semenova[1], and K. Yvind[1]

[1]*DTU Fotonik - Department of Photonics Engineering, Technical University of Denmark, 2800 Kgs. Lyngby, Denmark*

[2]*DTU Cen - Center for Electron Nanoscopy, Technical University of Denmark, 2800 Kgs. Lyngby, Denmark*

[3]*DTU Physics, Technical University of Denmark, Technical University of Denmark, 2800 Kgs. Lyngby, Denmark*

[*] Corresponding author. Tel.: +45 45256389. *E-mail address:* *ikul@fotonik.dtu.dk* (I. V. Kulkova)

Abstract

In this paper, we demonstrate the applicability of MOVPE butt-joint regrowth for integration of all-active InP/AlGaAs/InGaAsP optical components and the realization of high-functionality compact photonic devices. Planar high-quality integration of semiconductor optical amplifiers of various epi-structures with a multi-quantum well electro-absorption modulator has been successfully performed and their optical and crystalline quality was experimentally investigated. The regrown multi-quantum well material exhibits a slight bandgap blue-shift of less than 20 meV, when moving away from the regrowth interface. In closest vicinity to the mask, the growth profile revealed a bent-up shape which is associated with an increase in the bandgap energy resulting from the combined effect of growth rate suppression and higher Ga concentration. This increase in bandgap energy makes the interface partially transparent (thus beneficial for unaffected light transmission) and forces carriers away from possible interfacial defects. The internal reflectivity below 2.1×10^{-5} ensures minimization of detrimental intracavity feedback.

Keywords: A3. Butt-joint scheme, A3. Selective area growth, A.3. Metalorganic vapor phase epitaxy, B2. AlGaInAs/InP

Introduction

Monolithic integration of semiconductor optical components has been developing intensively from the early 80s and has been successfully implemented for fabrication of buried heterostructure lasers and photonic integrated circuits for telecommunications applications based on the conventional InP-based InGaAsP and AlGaInAs material systems [1]. The possibility of using AlGaInAs compounds greatly improves device performance due to the favorably high band offset for electrons (e.g. [2], [3]), while the butt-joint regrowth (BJR) technique offers maximum design flexibility for further boosting the capabilities of integrated devices by allowing independent choices of material structures for each component. However, monolithic integration of AlGaInAs-based devices has been limited due to the strong tendency of Al-containing alloys to oxidize. Improvements in the precursor purity, namely trimethylaluminum and trimethylindium, as well as in the quality of the equipment employed for metalorganic vapour phase epitaxy (MOVPE) in the past decades have made possible the growth of high-quality Al containing layers [4]. In case of BJR, the process requires partial removal of an as-grown material covered with a dielectric mask, followed by non-planar selective area growth (SAG). Mesa sidewalls composed of AlGaInAs material and exposed to air may result in AlOx formation, and hence cause interface imperfections, giving rise to excessive insertion losses and intracavity reflection. In particular, minimizing reflection back to the waveguide is of high importance for stable operation of integrated waveguide devices. Even a small internal reflectivity leads to lasing wavelength instability and frequency chirp in distributed-feedback lasers integrated with electroabsorption modulators (EAMs) [5]–[7]. This is more crucial for monolithic mode-locked lasers (MLLs), which are used as compact sources for ultrashort optical pulses and are composed of a semiconductor optical amplifier (SOA) and a saturable absorber. Such an optical feedback leads to detrimental multicavity effects, for instance the multipulsing regime reported in [8]. An acceptable level of reflectivity, e.g. for MLLs, has been estimated to be below 10^{-5} [9]. To our knowledge, the lowest reported reflectivity between integrated active optical components of about 10^{-5} per interface was obtained by realizing an angled interface [10], while exhibiting high internal losses of 1.5 dB. In comparison, a reflectivity down to 0.5×10^{-5} and 0.46 dB losses were demonstrated for active – passive integration in [11]. Thus, achievement of low internal reflectivity along with high mode coupling is required for fabrication of the next-generation optical devices. Another issue is related to the increased demands on more functionality along with compactness, and therefore on the composition uniformity and associated invariability of optical properties when all-active integration is performed. Moreover, flat and defect-free regrowth interface is necessary for avoiding additional light scattering and essential for the technological aspects of further device processing.

In this paper, we describe a versatile MOVPE regrowth process based on three step etching for mesa preparation, which was successfully utilized for the integration of a quantum well (QW) and (quantum dots) QDs based SOA and MQW EAM. Laterally planar butt-coupling interfaces are demonstrated for SOA structures with symmetric and asymmetric waveguide cores, consisting of InP/AlGaInAs/InGaAsP layers. The investigation of optical properties at the interface is carried out with the support of structural and compositional analysis. We demonstrate that low intracavity reflection and reduced carrier losses can be achieved for this integrated material.

2. Experiment

In order to investigate the BJR of active components we integrated a QW SOA structure with a MQW EAM relying on the quantum-confined Stark effect for operation in the 1.55 μm telecommunications range. The QW SOA consisted of a single compressively strained QW embedded in asymmetric AlGaInAs /InGaAsP waveguide (WG) layers. For the fast EAM, eight shallow tensile strained QWs in a stepped InGaAsP WG core were used. A detailed description of the epitaxial structures is presented in Table 1. The thicknesses of the WG layers were optimized by calculating the TE fundamental mode profiles resulting in mode coupling better than 99.7%, assuming a 2 μm wide ridge.

Growth was carried out on InP (100) substrates using a low-pressure (60 Torr) Turbodisc® MOVPE system with trimethylindium, trimethylgallium, trimethylaluminum, arsine and phosphine as main precursors, disilane and diethyl zinc as dopant precursors and hydrogen as carrier gas. Both initial growth and following regrowth were performed at standard growth conditions for the system offering maximal flexibility in design of epi-structures. The growth temperature was 610°C for InGaAsP and 650°C for AlGaInAs alloys. The V/III molar flow ratio ranged from 80 for InGaAs to 145 for InP. Growth rates for InGaAsP alloys were measured between 0.5 nm/s for InP and 1.0 nm/s for (Al)InGaAs.

First, the SOA structure was grown and patterned with a SiO_2 mask by means of conventional photolithography and CHF_3/O_2 reactive-ion etching (RIE). The mask layout consisted of 20 μm wide stripes oriented along the laser waveguide [011] direction. The end edge of each stripe was angled 30° towards [0-11], as depicted in the inset of Fig. 1(b), in order to minimize back reflection from the interface. After patterning, the unprotected SOA material was etched by non-selective $Cl_2/CH_4/Ar$ inductively coupled plasma RIE (ICP-RIE) down to the InP buffer layer to form vertical mesa blocks. This was followed by anisotropic selective wet etching in 1 HCl : 4 H_3PO_4 of the buffer down to a sacrificial etch stop layer. Thus, a damage-free and smooth surface required for epitaxial growth was produced. The etch-stop layer ensured precise vertical alignment with the regrown EAM structure. Moreover, etching revealed {211} planes bounded to the base. The second wet etching with 1 H_2SO_4 : 8 H_2O_2 : 80 H_2O was applied to recess AlGaInAs and InGaAsP compounds selectively, and, thereby create a mask undercut in a controllable manner. The resulting mesa profile is presented in Fig. 1(a).

Prior to the second growth, the wafer was cleaned in oxygen plasma and etched in concentrated H_2SO_4 for 5 min to remove any organic contamination, surface damage, and native oxide layer, and as shown in [12], to reduce carbon incorporation. To promote deoxidation of the residual AlO_x, the cleaning procedure was completed by a standard pre-growth heating at 650°C in the MOVPE chamber under PH_3 atmosphere. The annealing time was 15 min, which we found to be sufficiently effective compared to the 45 min recommended in [13]. The final mesa profile after annealing is depicted in Fig. 1(b). Subsequently, the growth of EAM layers was performed.

In addition to the lateral vapor phase diffusion and surface migration effects attributed to MOVPE growth on patterned and non-planar substrates (see e.g. [14]–[16]), the growth morphology and material distribution at the BJR interface can be affected by the mesa topology. In order to investigate the growth evolution, the QW SOA was regrown with a test structure consisting of a 50 nm InP buffer layer and a stack of repeating 50 nm thick InP and lattice-matched InGaAs for a total thickness of 950 nm, which is significantly thicker than the etched depth plus mask. In order to examine microscopic changes in the vicinity to the mask, we employed scanning electron microscopy (SEM) and scanning transmission electron microscopy (STEM) imaging. The elemental analysis was performed using energy dispersive X-ray spectroscopy (EDS) carried out in STEM. Our STEM and EDS analyses were carried out on an approximately 100 nm thick lamella prepared in the direction perpendicular to the angled mask edge, as shown in the inset of Fig. 1(b), using focused ion beam milling.

In order to validate the versatility of the approach, another type of SOA with a symmetric InGaAsP core and three layers of InAs QDs capped with GaAs in an InGaAsP matrix was regrown with the EAM using the given description. The epitaxial structure is detailed in Table 1 and the growth conditions can be found in [17].

The optical properties of the SOA and EAM material were evaluated at room temperature by confocal μ-PL spectroscopy with a ~ 1.5 μm detection spot size (NA=0.9) using a 980 nm CW laser diode as the excitation light source. In order to obtain gain and loss spectra and thereby deduce information on the interface reflectivity and losses, electrically-pumped multi-contact 2 μm wide ridge waveguide devices including a number of BJR interfaces were used. For this purpose, the integrated QW SOA - MQW EAM structure was overgrown with a 2 μm thick p-doped InP cladding and InGaAsP and InGaAs contact layers. The devices were fabricated using a conventional process flow for ridge waveguide lasers. The electrical isolation between sections was obtained by etching through the highly doped contact layers in 5 μm wide separation gaps, resulting in ~ 3 - 10 kΩ resistance between sections. Individual devices were cleaved and soldered epi-side up to AlN heatsinks.

3. Results and discussion

a) Regrowth profile

Fig. 2(a) shows the cross-sectional STEM image of the regrowth profile of the InGaAs/InP multilayer stack projected along the [013] crystallographic direction. At the first stage of the regrowth, below the mask level near the mesa edge (marker A), growth tends to occur with the formation of {311} or high index growth planes, such as {511}, {711}, etc., consisting of longer {100} terraces interleaved with {111}A steps, which are initiated by the exposed {211} facets at the bottom, and increased concentration of source molecules arriving from the dielectric mask. The growth of InGaAs is decreased by a factor of 0.85 (on average), as seen from Fig. 2(b) for the markers A and B, which is consistent with [18]. Further from the interface (from marker C to E and F), the [100] direction becomes dominant, and the growth rate increases to the nominal value. InP layers grow 1.8 times faster (on average) on the inclined facets (markers A and B) than on (100), which leads to the material pile-up observed within a 1 μm range from the mask. Above the mask level, the InGaAs layers form trapezoidal prisms terminated by the slowly developing {311} facets (marker D), while the InP growth displays a planarizing effect and, thus, a more smooth topology. This distinctive behavior was found to be in good agreement with the growth of InP and InGaAs on non-planar substrates reported in [14], where the tendency of InGaAs to restore low index planes during growth was also demonstrated.

The EDS compositional analysis showed an increase in Ga concentration by a few percent near the mask edge (Fig. 2(b), markers A – E), while In-rich material is generally observed due to the shorter surface migration length [18]–[20]. Indeed, the Ga incorporation rate can be enhanced compared to that of In for the growth of alloys with a higher As fraction, as demonstrated in [21]. Moreover, non-planar growth is strongly dependent on the local differences in surface energy, e.g. attributed to the curvature in the undercut cavity, surface states, strain, etc. Minimization of the potential is the driving force for atom incorporation. Thus, the highest deviation of the InGaAs composition of 0.045 in mole fraction (equivalent to 0.34% in-plane strain) with respect to the nominal value was measured closest to the interface (marker A) and the bent areas (marker C), which is assumed to compensate the curvature effect. Comparing the A and B markers of the similar topology, strain reduction is clearly observed for overlying layers.

The most pronounced material perturbation occurs in the area of mask undercut and directly at the interface as displayed in the inset of Fig. 2(a). The red contour outlines the mesa profile shown in Fig. 1(b). During the growth of the first layers (~ 200 nm in this case), the filling of the mask underetch occurs. The following layers restore a bent-up profile. The smeared intensity profiles of the InP/InGaAs interfaces in STEM images and the compositional profiles in the EDS spectra can be attributed to the spatially shifted transient interface region within the lamella due to a misalignment of ~3.4º between the mask edge and the crystallographic direction chosen for STEM as shown in the inset of Fig. 1(b)), as well as providing evidence for interfacial material intermixing [22]. Promisingly, no dislocations caused by phase segregation or related to oxidation of the AlGaInAs layer could be observed.

The growth rate enhancement (GRE) of approximately 1.14% on the {100} planes for both InP and InGaAs layers near the interface (markers E, F), is associated with diffusion of the precursors in the vapor phase from the masked area inherent to the SAG process. This effect vanishes gradually within a few tens of microns as determined by 3D optical interference profiling.

The discovered tendency of the compositional dependency of growth rate was used to suppress mask overgrowth by controlling the ratio between the deposited InP and quaternaries and by adjusting the undercut volume. In Fig. 3 we present SEM images of the optimized butt-coupled interfaces between the asymmetric waveguide QW SOA (a) and symmetric waveguide QD SOA (b) and MQW EAM in the [011] direction. To enhance the contrast the samples were stain etched with 1 H_2SO_4 : 8 H_2O_2 : 80 H_2O. The surface non-planarity for both epi-structures was measured

to be below 100 nm. No voids for large overhangs above 0.8 μm in depth (Fig. 3(b) Inset) were observed. Consistently with the InP/InGaAs test regrowth, the resulting EAM profile is bending up by ~ 500 nm at the interface with drastic reduction of the QWs and cladding layer thicknesses.

b) Micro-photoluminescence measurements

The μ-PL spectral map of the integrated QW SOA and EAM structure (see SEM image in Fig. 3(a)) is presented in Fig. 4(a). The spectra labeled SOA and EAM show the reference PL signal taken at points a few tens of microns away from the mask edge, where the mask proximity effects can be neglected. The emission from the as-grown SOA section exhibits abrupt intensity cutoff at the interface. The PL peaks centered at ~ 1475 nm are broadened towards shorter wavelengths due to the high carrier density within the 3.4 nm QW at high optical excitation (3 mW). For comparison, the left diagram (labeled "SOA *Low* P_{Ex}") shows the SOA spectrum at a lower excitation power (0.14 mW), resulting in a peak position at 1485 nm. The lasing wavelength from a 4 mm edge-emitting laser made from this material was measured as 1535 nm, which is due to fast band filling in such a narrow QW and low output losses.

The MQW EAM PL peak intensity grows smoothly and reaches its half-maximum value at 1 μm away from the interface, as depicted in Fig. 4(b). In total the peak wavelength blue-shifts by approximately 30 nm (17 meV) with respect to the reference level. The shift is induced by the complex change in the composition and width of QWs and barriers, schematically represented in Fig. 5 for points labeled in Fig. 4(a). The magnitude of the changes was evaluated from the STEM results (Fig. 2). However, due to modulations both laterally and in the QW stack, a rough quantitative estimation is provided.

The slow reduction of the PL peak wavelength by 15 nm (8.5 meV) over a few tens of microns (Fig. 5 "F" – "far") is in agreement with a growth rate enhancement of about 1.15. The composition change, as determined by EDS, is negligibly small in this range. Approaching the mask, the PL peak wavelength increases faster accompanied by moderate broadening for longer wavelengths. At the same time, according to the EDS data, the Ga content increases, which will have the opposite effect on the bandgap shift. When the Ga fraction in the QW increases, the strain and, therefore, the separation between light and heavy holes (LH and HH) states become larger as schematically shown in Fig. 5 ("E" – "F"). The contribution of the electron - light hole pair recombination becomes more pronounced, which can lead to the PL red-shift and broadening. Assuming the tensile strain of about 1% (+4% of Ga with respect to the nominal composition) in combination with the quantum confinement effect results in the energy separation of less than 25 meV which is in agreement with experimental data in [23].

In the range of approximately 500 nm from the interface (marker "A" in Fig. 2, Fig. 4 – 5), growth of InGaAs is drastically reduced due to surface faceting, as mentioned before, and the QW energy level separation is higher. Driven by the bandgap variation, the carriers move toward the narrow-bandgap material thereby lowering their energy; the migration length of a few microns can be assumed. Thus, the PL intensity can be suppressed due to the carrier out-diffusion from the excitation area, while the integrated power in the region adjacent to the interface is higher, as shown in Fig. 4(b). The fraction of carriers lost estimated from the integrated intensity is around 30%.

Another important effect causing carrier losses at the interface is non-radiative recombination at the deep-level recombination centers due to crystal defects. To verify the crystalline quality at the interface, we measured leakage current by applying high reverse bias through multi-section devices of equal geometry, with and without BJ coupled SOA-EAM structures. At high defect density, the leakage current rises rapidly and may cause shorting of the p-n junction and device failure. The absence of breakdown was detected up to -9 V allowing for wide-band absorption modulation [24]. The dark current was below 20 nA at 0 – -5V for all devices, proving good crystalline quality.

c) Internal reflectivity and coupling losses

Coupling losses were extracted from the lasing threshold condition for multiple butt-jointed lasers [25]. Gain and absorption coefficients and the internal waveguide losses were measured on the same wafer using a segmented contact method [26] and the spectra found in [24]. Thus, the coupling loss contribution was calculated for the devices with one and three BJR interfaces to be 1.10 ± 0.09 dB per interface, which is 0.4 dB better than that reported for an optimized SOA-EAM structure in [10]. However, this value is still twice the value obtained in 2D finite-difference time-domain simulation for a similar "up-bent" morphology [10]. An additional lateral deflection for our BJR structure can be expected due to the angled SAG mesa and sidewall roughness owing to ICP-RIE mesa etching under non-optimized etching parameters.

Internal reflection was obtained by measuring amplified spontaneous emission spectra with a resolution of 0.01 nm and detecting spectral modulation based on the Hakki-Paoli technique [27] presented in [28]. The test devices consisted of a 2 mm long section based on either the SOA or EAM material as a source of amplified spontaneous emission of TE or primary TM polarization, respectively. On each side an amplifying section was integrated with 350 μm long waveguide of the opposite type of active material. The waveguides were 10° tilted and antireflection coated to reduce external reflection from the output facets. No electrical contacts were formed on the 350 μm waveguide sections and they were consequently absorbing. The spectral variation of the gain and absorption coefficient is assumed to be constant within the detected range of a few nanometers. The recorded modulation depth for both SOA and EAM material was below the accuracy of the amplitude measurements defined as 0.02 dB for our setup. The TE reflection was determined to be lower than 6.2×10^{-4} for the maximum achieved SOA gain coefficient of 3.1 cm^{-1} in the presence of the absorbing EAM arms. The TM amplification provided in the EAM section was about 22 cm^{-1}. However, the modulation was not resolved and the reflectivity for the TM mode was estimated to be below 2.1×10^{-5} which is assumed to be larger than the real TE reflection.

4. Summary and conclusions

We demonstrated planar high-quality BJR integration of QD and QW SOAs with MQW EAM based on an InP/AlInGaAs/InGaAsP platform and analyzed the influence of the growth morphology, thickness and compositional variation associated with BJR process on the optical quality of MQW EAM. Spatially resolved micro-PL measurements showed a small bandgap blue-shift of less than 20 meV over tens of microns from the regrowth interface. The result was found to be in good agreement with the changes in thickness and composition obtained by STEM and EDS analyses. The bent up growth profile found on the EAM structure exhibits an increase in the energy bandgap directly at the interface, which is favorable for avoiding uncontrollable absorption, and ensured a reflectivity lower than 2×10^{-5}, as required to prevent intracavity feedback. The resulting deflection of the light out of the waveguide contributes to coupling optical losses estimated to be 1.1 dB per interface. Therefore, our complete examination of the properties of the regrowth interface, which are critical for achieving high device performance, demonstrates high promise for the fabrication of compact integrated devices.

Acknowledgments

The authors are grateful to Matthew Haines for working on ICP-RIE process optimization. This work was performed within the FLASH project supported by the Danish research council for technology and production and the Villum Kann Rasmussen foundation Center of Excellence: Nanophotonics for Terabit Communication (NATEC). ESS thanks the European Commission for funding through the Marie Curie Incoming International Fellowship (project number 252890).

References

[1] J. W. Raring, M. N. Sysak, A. Tauke-Pedretti, M. Dummer, E. J. Skogen, J. S. Barton, S. P. DenBaars, and L. A. Coldren, "Advanced Integration Schemes for High-Functionality/High- Performance Photonic Integrated Circuits," *Proc. SPIE*, vol. 6126, p. 61260H, Feb. 2006.

[2] C. E. Zah, R. Bhat, F. J. Favire, M. Koza, T. P. Lee, D. Darby, D. C. Flanders, and J. J. Hsieh, "Low threshold 1.3 um strained-layer AIxGayIn1-x-yAs quantum well lasers," *Electron. Lett.*, vol. 28, no. 25, p. 2323, 1992.

[3] W. Kobayashi, M. Arai, T. Yamanaka, N. Fujiwara, T. Fujisawa, T. Tadokoro, K. Tsuzuki, Y. Kondo, and F. Kano, "Design and Fabrication of 10-/40-Gb/s, Uncooled Electroabsorption Modulator Integrated DFB Laser With Butt-Joint Structure," *J. Light. Technol.*, vol. 28, no. 1, pp. 164–171, Jan. 2010.

[4] S. A. Rushworth, L. M. Smith, M. S. Ravetz, K. M. Coward, R. Odedra, R. Kanjolia, S. W. Bland, F. Dimroth, and A. W. Bett, "Correlation of reduced oxygen content in precursors with improved MOVPE layer quality," *J. Cryst. Growth*, vol. 248, pp. 86–90, Feb. 2003.

[5] R. W. Tkach and A. R. Chraplyvy, "Regimes of feedback effects in 1.5 um distributed feedback lasers," *J. Light. Technol.*, vol. 4, no. 11, pp. 1655–1661, 1986.

[6] Y. Kawamura, K. Wakita, and H. Asahi, "Monolithic Integration of a DFB Laser and an MQW Optical Modulator in the 1.5 um Wavelength Range," *IEEE J. Quantum Electron.*, vol. QE-23, no. 6, pp. 915–918, 1987.

[7] A. Lestra and P. Brosson, "Design Rules for a Low-Chirp Integrated DFR Laser with an Electroabsorption Modulator," *IEEE Photonics Technol. Lett.*, vol. 8, no. 8, pp. 998–1000, 1996.

[8] R. Scollo, H. Lohe, F. Robin, D. Erni, E. Gini, and H. Jäckel, "Mode-Locked InP-Based Laser Diode With a Monolithic Integrated UTC Absorber for Subpicosecond Pulse Generation," *IEEE J. Quantum Electron.*, vol. 45, no. 4, pp. 322–335, 2009.

[9] M. Schell, A. G. Weber, E. Scholl, and D. Bimberg, "Fundamental Limits of Sub-ps Pulse Generation by Active Mode Locking of Semiconductor Lasers : The Spectral Gain Width and the Facet Reflectivities," *IEEE J. Quantum Electron.*, vol. 27, no. 6, pp. 1661–1667, 1991.

[10] H.-J. Lohe, R. Scollo, W. Vogt, E. Gini, F. Robin, D. Erni, R. Harbers, and H. Jäckel, "A Multiple Regrowth Process for Monolithically-Integrated InP-Based Mode-Locked Laser Diodes with Uni-Travelling Carrier Absorber," *Proc. SPIE*, vol. 6183, p. 61831K, Apr. 2006.

[11] T. Brenner, R. Dall'Ara, C. Holtmann, P. A. Besse, and H. Melchior, "High gain low reflectivity travelling wave semiconductor optical amplifiers integrated with passive waveguides operating at 1.3 μm wavelength," in *IEEE (5th) International Conference on Indium Phosphide and Related Materials*, 1992, pp. 88–90.

[12] Y. Sun, Z. Liu, F. Machuca, P. Pianetta, and W. E. Spicer, "Optimized cleaning method for producing device quality InP(100) surfaces," *J. Appl. Phys.*, vol. 97, no. 12, p. 124902, 2005.

[13] Y. Takino, M. Shirao, N. Sato, T. Sato, T. Amemiya, N. Nishiyama, and S. Arai, "Improved Regrowth Interface of AlGaInAs/InP-Buried-Heterostructure Lasers by In-Situ Thermal Cleaning," *J. Quantum Electron.*, vol. 48, no. 8, pp. 971–979, 2012.

[14] B. Garrett and E. J. Thrush, "Temporally resolved growth habit studies of InP/(InGa)As heterostructures grown by MOCVD on contoured InP substrates," *J. Cryst. Growth*, vol. 97, pp. 273–284, 1989.

[15] D. G. Coronell and K. F. Jensen, "Analysis of MOCVD of GaAs on patterned substrates," *J. Cryst. Growth*, vol. 114, pp. 581–592, 1991.

[16] R. Bhat, "Current status of selective area epitaxy by OMCVD," *J. Cryst. Growth*, vol. 120, no. 1–4, pp. 362–368, May 1992.

[17] E. S. Semenova, I. V. Kulkova, S. Kadkhodazadeh, M. Schubert, and K. Yvind, "Metal organic vapor-phase epitaxy of InAs/InGaAsP quantum dots for laser applications at 1.5 μm," *Appl. Phys. Lett.*, vol. 99, no. 10, p. 101106, 2011.

[18] M. Gibbon, J. P. Stags, C. G. Cureton, E. J. Thrush, C. J. Jones, R. E. Mallard, R. E. Pritchard, N. Collis, and A. Chew, "Selective-area low-pressure MOCVD of GaInAsP and related materials on planar InP substrates," *Semicond. Sci. Technol*, pp. 998–1010, 1993.

[19] T. Shioda, M. Sugiyama, Y. Shimogaki, and Y. Nakano, "Vapor phase diffusion and surface diffusion combined model for InGaAsP selective area metal–organic vapor phase epitaxy," *J. Cryst. Growth*, vol. 298, pp. 37–40, Jan. 2007.

[20] N. Dupuis, J. Decobert, P. Y. Lagree, N. Lagay, C. Cuisin, F. Poingt, A. Ramdane, and C. Kazmierski, "AlGaInAs selective area growth by LP-MOVPE : experimental characterisation and predictive modelling," *IEEE Proc.-Optoelectron*, vol. 153, no. 6, pp. 276–279, 2006.

[21] J. E. Greenspan, "Alloy composition dependence in selective area epitaxy on InP substrates," *J. Cryst. Growth*, vol. 236, no. 1–3, pp. 273–280, Mar. 2002.

[22] S. Kadkhodazadeh, "High resolution STEM of quantum dots and quantum wires.," *Micron*, vol. 44, pp. 75–92, Jan. 2013.

[23] J. Jin, J. Shi, and D. Tian, "Optimization of InGaAsP–InP tensile strained multiple quantum-well structures emitting at 1.34 μm," *Semicond. Sci. Technol.*, vol. 19, no. 6, pp. 742–746, Jun. 2004.

[24] I. V Kulkova, D. Larsson, E. S. Semenova, and K. Yvind, "Individual optimization of InAlGaAsP-InP sections for 1.55-μm passively mode-locked lasers," in *IEEE International Semiconductor Laser Conference*, 2012, vol. 30, pp. 133–134.

[25] T. Kitatani, K. Shinoda, T. Tsuchiya, H. Sato, K. Ouchi, H. Uchiyama, S. Tsuji, and M. Aoki, "Evaluation of the optical-coupling efficiency of InGaAlAs-InGaAsP butt joint using a novel multiple butt-jointed laser," *IEEE Photonics Technol. Lett.*, vol. 17, no. 6, pp. 1148–1150, Jun. 2005.

[26] P. Blood, G. M. Lewis, P. M. Smowton, H. Summers, J. Thomson, and J. Lutti, "Characterization of semiconductor laser gain media by the segmented contact method," *IEEE J. Sel. Top. Quantum Electron.*, vol. 9, no. 5, pp. 1275–1282, Sep. 2003.

[27] B. W. Hakki and T. L. Paoli, "Gain spectra in GaAs double−heterostructure injection lasers," *J. Appl. Phys.*, vol. 46, no. 3, p. 1299, 1975.

[28] Y. Barbarin, E. a. J. M. Bente, C. Marquet, E. J. S. Leclere, J. J. M. Binsma, and M. K. Smit, "Measurement of reflectivity of butt-joint active-passive interfaces in integrated extended cavity lasers," *IEEE Photonics Technol. Lett.*, vol. 17, no. 11, pp. 2265–2267, Nov. 2005.

Figures and Tables

Table 1. Epitaxial structure of the QW SOA, QD SOA and EAM integrated sections

	QW SOA @ 1.55 µm	QD SOA @ 1.55 µm	MQW EAM @ 1.46 µm
Buffer	50 nm InP		120 nm InP
p-WG	235 nm $Ga_{0.15}In_{0.85}As_{0.32}P_{0.68}$	160 nm $Ga_{0.15}In_{0.85}As_{0.32}P_{0.68}$	50 nm $Ga_{0.15}In_{0.85}As_{0.32}P_{0.68}$ 50 nm $Ga_{0.28}In_{0.72}As_{0.61}P_{0.39}$
Active layers and barriers	20 nm $Al_{0.48}In_{0.52}As$ 3.4 nm $In_{0.8}Ga_{0.2}As$ 10 nm InP	3x 30nm $Ga_{0.15}In_{0.85}As_{0.32}P_{0.68}$ QD 1.65ML InAs + 1.7 ML GaAs 30nm $Ga_{0.15}In_{0.85}As_{0.32}P_{0.68}$	8x 6.6 nm $Al_{0.16}Ga_{0.25}In_{0.59}As$ 8.6 nm $In_{0.46}Ga_{0.54}As$ 6.6 nm $Al_{0.16}Ga_{0.25}In_{0.59}As$
n-WG	235 nm $Al_{0.33}Ga_{0.143}In_{0.53}As$	160 nm $Ga_{0.15}In_{0.85}As_{0.32}P_{0.68}$	50 nm $Ga_{0.15}In_{0.85}As_{0.32}P_{0.68}$
Buffer	250 nm InP		350 nm InP
Etch Stop	10 nm $Ga_{0.15}In_{0.85}As_{0.32}P_{0.68}$		
Substrate	n^+-InP		

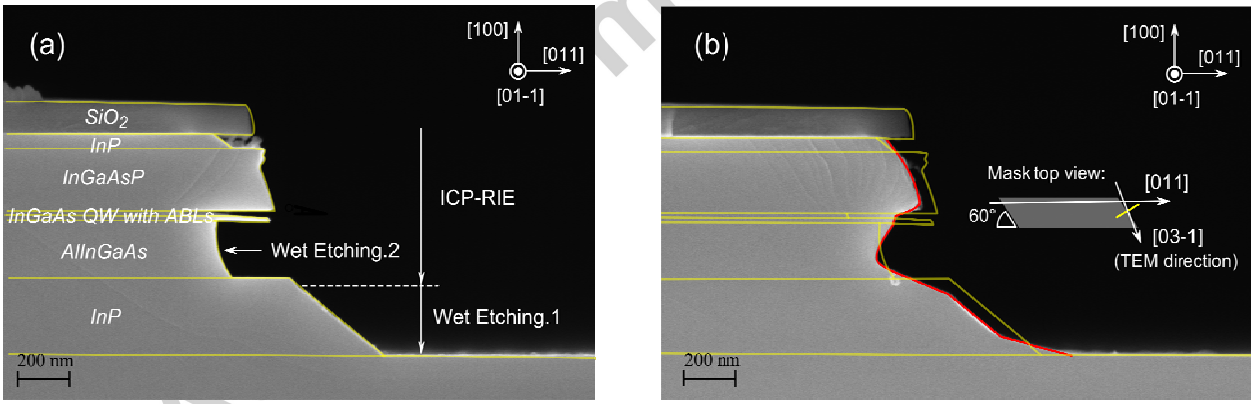

Fig. 1. SEM images of the cross-section of a single QW SOA mesa block before (a) and after (b) *in-situ* annealing at 650°C for 15 min. Inset to (b): mask layout.

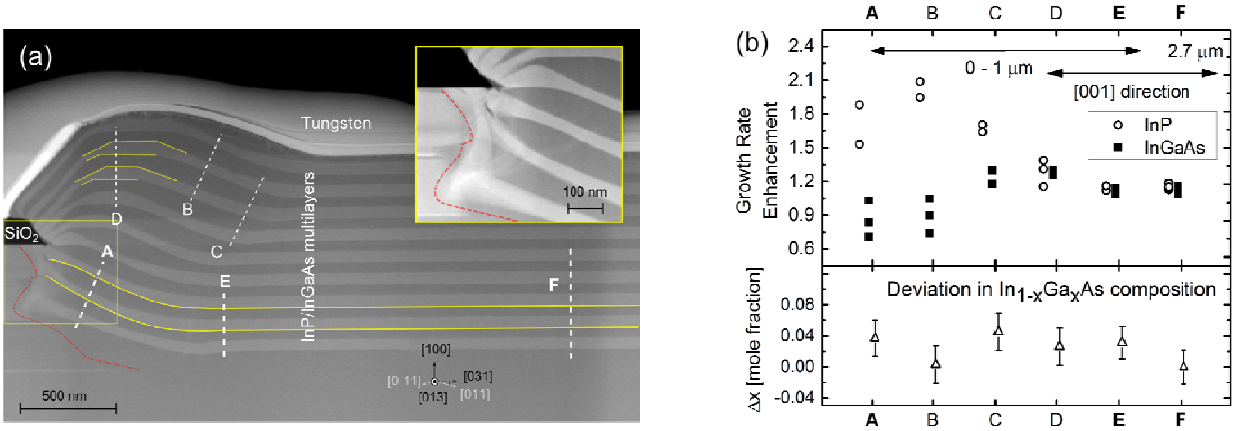

Fig. 2. (a) Cross-sectional STEM image of the InP/InGaAs test structure integrated with the QW SOA (Inset: BJ interface). The red dashed line shows the SOA mesa profile before regrowth. (b) Growth rate and absolute group III composition deviation of Ga in $In_{1-x}Ga_xAs$ from the nominal one obtained from EDS analysis at different points marked in the STEM image in (a). The error bars show the EDS experimental deviations with the average uncertainty of 4.5 ± 0.3%.

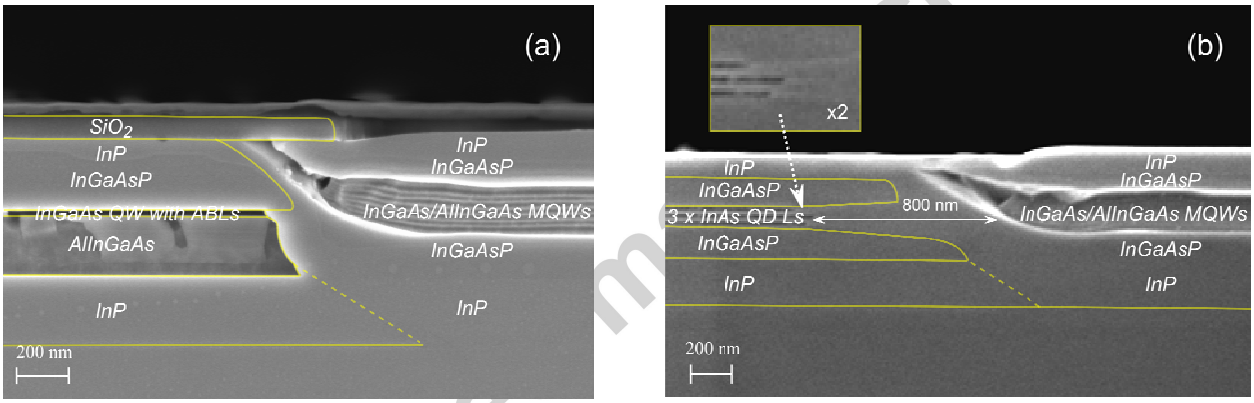

Fig. 3. SEM images of BJR interfaces between the single QW SOA (a) and 3 layer QD SOA (b) with the MQW EAM.

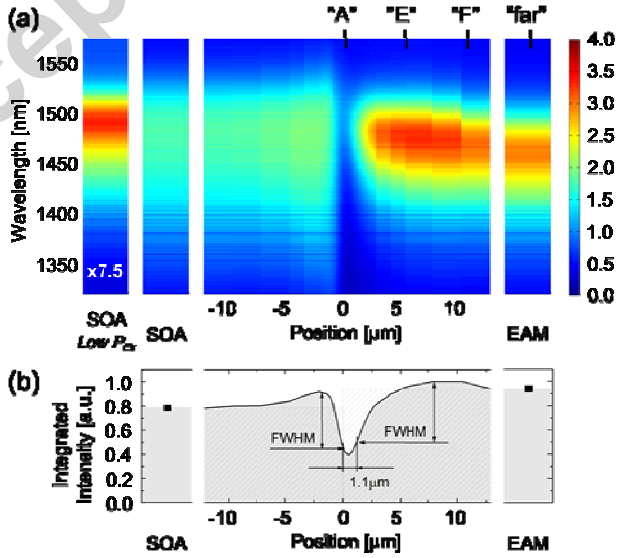

Fig. 4. (a) Color map of RT μ-PL spectra of the QW SOA and EAM acquired along the [011] direction and (b) the corresponding profile of the PL intensity integrated over energy.

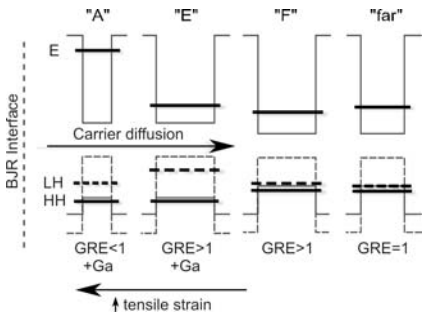

Fig. 5. Schematic of a QW energy band structure illustrating BJR-induced changes expected in the MQW material. The solid and dashed lines represent the light hole (LH) and heavy hole (HH) ground state positions, respectively. The letters refer to those marked in Fig. 2 and Fig. 4.

Research highlights

- No detrimental effects from butt-joint regrowth on AlInGaAs found using proper pre-treatment.
- Detailed investigations of compositional and thickness variation at the interface.
- Data analysis combined with micro-PL, and electro-optical properties of the material.
- Favorable increased energy bandgap at the interface reduces non-radiative recombination.